

# Using Tabulated Experimental Data to Drive an Orthotropic Elasto-Plastic Three-Dimensional Model for Impact Analysis

C. Hoffarth, B. Khaled and S. D. Rajan

*School of Sustainable Engineering and the Built Environment, Arizona State University, Tempe, AZ 85287*

R. Goldberg and K. Carney

*NASA-GRC, Cleveland, OH*

P. DuBois

*George Mason University, Fairfax, VA*

Gunther Blankenhorn

*LSTC, Livermore, CA*

## Abstract

*An orthotropic elasto-plastic-damage three-dimensional model with tabulated input has been developed to analyze the impact response of composite materials. The theory has been implemented as MAT 213 into a tailored version of LS-DYNA<sup>®</sup> being developed under a joint effort of the FAA and NASA and has the following features: (a) the theory addresses any composite architecture that can be experimentally characterized as an orthotropic material and includes rate and temperature sensitivities, (b) the formulation is applicable for solid as well as shell element implementations and utilizes input data in a tabulated form directly from processed experimental data, (c) deformation and damage mechanics are both accounted for within the material model, (d) failure criteria are established that are functions of strain and damage parameters, and mesh size dependence is included, and (e) the theory can be efficiently implemented into a commercial code for both sequential and parallel executions. The salient features of the theory as implemented in LS-DYNA are illustrated using a widely used composite – the T800S/3900-2B[P2352W-19] BMS8-276 Rev-H-Unitape fiber/resin unidirectional composite. First, the experimental tests to characterize the deformation, damage and failure parameters in the material behavior are discussed. Second, the MAT213 input model and implementation details are presented with particular attention given to procedures that have been incorporated to ensure that the yield surfaces in the rate and temperature dependent plasticity model are convex. Finally, the paper concludes with a validation test designed to test the stability, accuracy and efficiency of the implemented model.*

## Introduction

An orthotropic plasticity material model that is driven by experimental data requires robust theory and computer implementation. In this paper, we discuss the implementation of an orthotropic elasto-plastic-damage three-dimensional model with tabulated input has been developed to analyze the impact response of composite materials. The theory has been implemented as MAT 213 into a tailored version of LS-DYNA being developed under a joint effort of the FAA and NASA and has the following features: (a) the theory addresses any composite architecture that can be experimentally characterized as an orthotropic material and includes rate and temperature sensitivities, (b) the formulation is applicable for solid as well as

shell element implementations and utilizes input data in a tabulated form directly from processed experimental data, (c) deformation and damage mechanics are both accounted for within the material model, (d) failure criteria are established that are functions of strain and damage parameters, and mesh size dependence is included, and (e) the theory can be efficiently implemented into a commercial code for both sequential and parallel executions.

The theory [Goldberg, 2015] requires the use of twelve distinct stress-strain curves. Denoting the principal material directions as 1, 2, and 3, the twelve curves include (i) tension curves in the 1, 2, and 3 directions, (ii) compression curves in the 1, 2, and 3 directions, (iii) shear tests in the 1-2, 2-3, and 3-1 planes, and (iv) tests to capture the interactive behavior between principal directions, e.g. 45° off-axis tension or compression tests in the 1-2, 2-3, and 1-3 principal material planes. If the composite exhibits rate and/or temperature dependencies, then these twelve curves must be generated at various temperature and rates.

The paper is divided into two parts. In the first part of the paper we discuss how we experimentally characterize a popular composite, the T800S/3900-2B[P2352W-19] BMS8-276 Rev-H-Unitape fiber/resin unidirectional composite [Toray, 2003]. The second part of the paper discusses the implementation and usage of the tabulated data as a part of MAT213 and a validation test used as a part of the implementation and quality assurance process.

### Creating Tabulated Experimental Data for MAT213

The MAT213 material model used in this study is a new three-dimensional orthotropic elasto-plastic model that was developed to be general enough to support a large variety of composite architectures. The elasto-plastic deformation in the model consists of a general orthotropic constitutive relationship, represented by orthotropic elastic stiffness matrix shown in Eq. (1).

$$\mathbf{C} = \mathbf{S}^{-1} = \begin{bmatrix} \frac{1}{E_{11}} & -\frac{\nu_{21}}{E_{22}} & -\frac{\nu_{31}}{E_{33}} & 0 & 0 & 0 \\ & \frac{1}{E_{22}} & -\frac{\nu_{32}}{E_{33}} & 0 & 0 & 0 \\ & & \frac{1}{E_{33}} & 0 & 0 & 0 \\ & & & \frac{1}{G_{23}} & 0 & 0 \\ & \text{Sym} & & & \frac{1}{G_{31}} & 0 \\ & & & & & \frac{1}{G_{12}} \end{bmatrix}^{-1} \quad (1)$$

The plasticity is governed by a Tsai-Wu yield surface to determine the initiation and evolution of plasticity, with the yield function defined as (Hoffarth et al., 2016; Goldberg et al., 2015)

$$f(\sigma) = a + (F_1 \ F_2 \ F_3 \ 0 \ 0 \ 0) \begin{bmatrix} \sigma_{11} \\ \sigma_{22} \\ \sigma_{33} \\ \sigma_{12} \\ \sigma_{23} \\ \sigma_{31} \end{bmatrix} + \begin{bmatrix} \sigma_{11} \\ \sigma_{22} \\ \sigma_{33} \\ \sigma_{12} \\ \sigma_{23} \\ \sigma_{31} \end{bmatrix}^T \begin{bmatrix} F_{11} & F_{12} & F_{13} & 0 & 0 & 0 \\ F_{12} & F_{22} & F_{23} & 0 & 0 & 0 \\ F_{13} & F_{23} & F_{33} & 0 & 0 & 0 \\ 0 & 0 & 0 & F_{44} & 0 & 0 \\ 0 & 0 & 0 & 0 & F_{55} & 0 \\ 0 & 0 & 0 & 0 & 0 & F_{66} \end{bmatrix} \begin{bmatrix} \sigma_{11} \\ \sigma_{22} \\ \sigma_{33} \\ \sigma_{12} \\ \sigma_{23} \\ \sigma_{31} \end{bmatrix} \quad (2)$$

where the  $F_{ij}$  coefficients represent the yield stress contribution in the different coordinate directions and the coefficient  $a = -1$  for unity at zero. The yield function coefficients are calculated based on the initial yield stress values to determine the onset of plasticity and updated based on the evolution of the yield stresses, calculated as

$$\begin{aligned} F_1 &= \frac{1}{\sigma_{11}^T} - \frac{1}{\sigma_{11}^C} & F_{11} &= \frac{1}{\sigma_{11}^T \sigma_{11}^C} & F_{44} &= \frac{1}{\sigma_{12}^2} \\ F_2 &= \frac{1}{\sigma_{22}^T} - \frac{1}{\sigma_{22}^C} & F_{22} &= \frac{1}{\sigma_{22}^T \sigma_{22}^C} & F_{55} &= \frac{1}{\sigma_{23}^2} \end{aligned} \quad (3)$$

$$\begin{aligned} F_3 &= \frac{1}{\sigma_{33}^T} - \frac{1}{\sigma_{33}^C} & F_{33} &= \frac{1}{\sigma_{33}^T \sigma_{33}^C} & F_{66} &= \frac{1}{\sigma_{31}^2} \\ F_{12} &= \frac{2}{(\sigma_{12}^{45})^2} - \frac{F_1 + F_2}{\sigma_{12}^{45}} - \frac{1}{2}(F_{11} + F_{22} + F_{44}) \end{aligned} \quad (4)$$

$$F_{23} = \frac{2}{(\sigma_{23}^{45})^2} - \frac{F_2 + F_3}{\sigma_{23}^{45}} - \frac{1}{2}(F_{22} + F_{33} + F_{55}) \quad (5)$$

$$F_{13} = \frac{2}{(\sigma_{31}^{45})^2} - \frac{F_1 + F_3}{\sigma_{31}^{45}} - \frac{1}{2}(F_{11} + F_{33} + F_{66}) \quad (6)$$

The evolution of the yield stresses shown in Eqns. (3),(4),(5) and (6) is characterized by the stress-strain curves in the corresponding material directions. The initial yield stresses are defined based on the user specified initial yield strain values and the elastic moduli values from Eq. (1) are calculated internally by the model as the correlated initial yield stress, divided by the user specified initial yield strain. Plasticity in MAT213 is non-associative requiring a separate flow surface, also known as a plastic potential function, and corresponding flow rule coefficients. The plastic potential function and description of the process for determining the coefficients is presented in (Goldberg et al., 2015), with the plastic potential defined as

$$h = \sqrt{H_{11}\sigma_{11}^2 + H_{22}\sigma_{22}^2 + H_{33}\sigma_{33}^2 + 2H_{12}\sigma_{11}\sigma_{22} + 2H_{23}\sigma_{22}\sigma_{33} + 2H_{31}\sigma_{33}\sigma_{11} + H_{44}\sigma_{12}^2 + H_{55}\sigma_{23}^2 + H_{66}\sigma_{31}^2} \quad (7)$$

where the  $H_{ij}$  terms represent the flow rule coefficients and the  $\sigma_{ij}$  terms are the current stresses in the material (not yield stresses). In short, the flow law is defined in terms of the plastic strain rate ( $\dot{\epsilon}^p$ ), plastic multiplier ( $\lambda$ ), plastic potential function ( $h$ ) and stresses ( $\sigma$ ) as

$$\begin{aligned}
 \dot{\boldsymbol{\varepsilon}}^p &= \dot{\lambda} \frac{\partial h}{\partial \boldsymbol{\sigma}} \\
 \dot{\varepsilon}_{11}^p &= \frac{\dot{\lambda}}{2h} (2H_{11}\sigma_{11} + 2H_{12}\sigma_{22} + 2H_{13}\sigma_{33}) \\
 \dot{\varepsilon}_{22}^p &= \frac{\dot{\lambda}}{2h} (2H_{12}\sigma_{11} + 2H_{22}\sigma_{22} + 2H_{23}\sigma_{33}) \\
 \dot{\varepsilon}_{33}^p &= \frac{\dot{\lambda}}{2h} (2H_{13}\sigma_{11} + 2H_{23}\sigma_{22} + 2H_{33}\sigma_{33}) \\
 \dot{\varepsilon}_{12}^p &= \frac{\dot{\lambda}}{2h} H_{44}\sigma_{12} \\
 \dot{\varepsilon}_{23}^p &= \frac{\dot{\lambda}}{2h} H_{55}\sigma_{23} \\
 \dot{\varepsilon}_{31}^p &= \frac{\dot{\lambda}}{2h} H_{66}\sigma_{31}
 \end{aligned} \tag{8}$$

where the plastic strains are related to the plastic Poisson's ratios  $\nu_{ij}^p$  as  $\nu_{ij}^p = -\frac{\dot{\varepsilon}_{ij}^p}{\dot{\varepsilon}_{ii}^p}$ , allowing for the determination of the flow rule coefficients based on the plastic Poisson's ratios. The required tests follows ASTM standards as closely as possible [ASTM, 2007; ASTM, 2008; ASTM, 2012; ASTM 2013; ASTM, 2014] and the resulting input for MAT213 are summarized in Table 1.

Table 1. Required tests and resulting input for MAT213 [Harrington et al., 2016]

Test	Description	ASTM Standard	Resulting Input for MAT213
T1	Tension 1-direction	D3039	Tension stress-strain curve $\sigma_{11}^T$ vs $\varepsilon_{11}^T$
			Yield strain $(\varepsilon_{11})_y^T$ and yield stress $(\sigma_{11})_y^T$
			Elastic Poisson's ratio $(\nu_{12}, \nu_{13})$
			Plastic Poisson's ratio $(\nu_{12}^p, \nu_{13}^p)$
T2	Tension 2-direction	D3039	Tension stress-strain curve $\sigma_{22}^T$ vs $\varepsilon_{22}^T$
			Yield strain $(\varepsilon_{22})_y^T$ and yield stress $(\sigma_{22})_y^T$
			Elastic Poisson's ratio $(\nu_{23})$
			Plastic Poisson's ratio $(\nu_{21}^p, \nu_{12}^p)$
T3	Tension 3-direction	D7291	Tension stress-strain curve $\sigma_{33}^T$ vs $\varepsilon_{33}^T$
			Yield strain $(\varepsilon_{33})_y^T$ and yield stress $(\sigma_{33})_y^T$
			Plastic Poisson's ratio $(\nu_{32}^p, \nu_{31}^p)$
T4	Compression 1-direction	D3410	Compression stress-strain curve $\sigma_{11}^C$ vs $\varepsilon_{11}^C$
			Yield strain $(\varepsilon_{11})_y^C$ and yield stress $(\sigma_{11})_y^C$

T5	Compression 2-direction	D3410	Compression stress-strain curve $\sigma_{22}^C$ vs $\epsilon_{22}^C$
			Yield strain $(\epsilon_{22})_y^C$ and yield stress $(\sigma_{22})_y^C$
T6	Compression 3-direction	D7291	Compression stress-strain curve $\sigma_{33}^C$ vs $\epsilon_{33}^C$
			Yield strain $(\epsilon_{33})_y^C$ and yield stress $(\sigma_{33})_y^C$
T7	Shear 1-2 plane	D5379/M-12	Shear stress-strain curve $\sigma_{12}$ vs $\epsilon_{12}$
			Yield strain $(\epsilon_{12})_y$ and yield stress $(\sigma_{12})_y$
T8	Shear 2-3 plane	D5379/M-12	Shear stress-strain curve $\sigma_{23}$ vs $\epsilon_{23}$
			Yield strain $(\epsilon_{23})_y$ and yield stress $(\sigma_{23})_y$
T9	Shear 1-3 plane	D5379/M-12	Shear stress-strain curve $\sigma_{31}$ vs $\epsilon_{31}$
			Yield strain $(\epsilon_{31})_y$ and yield stress $(\sigma_{31})_y$
T10	Off-axis tension (45 <sup>0</sup> , 1-2 plane)	D3039	Off-axis tension stress-strain curve $\sigma_{45}^{1-2}$ vs $\epsilon_{45}^{1-2}$
			Yield strain $(\epsilon_{45}^{1-2})_y$ and yield stress $(\sigma_{45}^{1-2})_y$
T11	Off-axis tension (45 <sup>0</sup> , 2-3 plane)	D3039	Off-axis tension stress-strain curve $\sigma_{45}^{2-3}$ vs $\epsilon_{45}^{2-3}$
			Yield strain $(\epsilon_{45}^{2-3})_y$ and yield stress $(\sigma_{45}^{2-3})_y$
T12	Off-axis tension (45 <sup>0</sup> , 1-3 plane)	D3039	Off-axis tension stress-strain curve $\sigma_{45}^{1-3}$ vs $\epsilon_{45}^{1-3}$
			Yield strain $(\epsilon_{45}^{1-3})_y$ and yield stress $(\sigma_{45}^{1-3})_y$

The experimental data are obtained using coupon testing on a hydraulic test frame. Load cells built into the test frames are used to obtain force data. Digital image correlation (DIC) is used to capture the strain field throughout the duration of the experiment. A few of these tests are discussed below.

**2-Direction Tension Test**

The specimen geometry and layout are shown in Fig. 1. The results are summarized in Fig. 2 and Table 2.

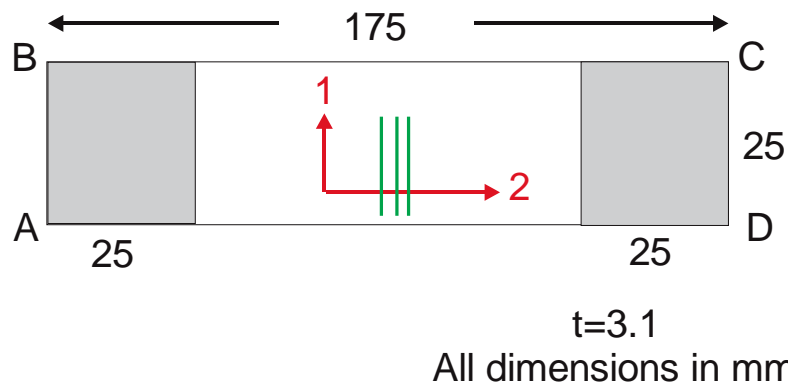


Fig. 1. Typical specimen geometry and layout

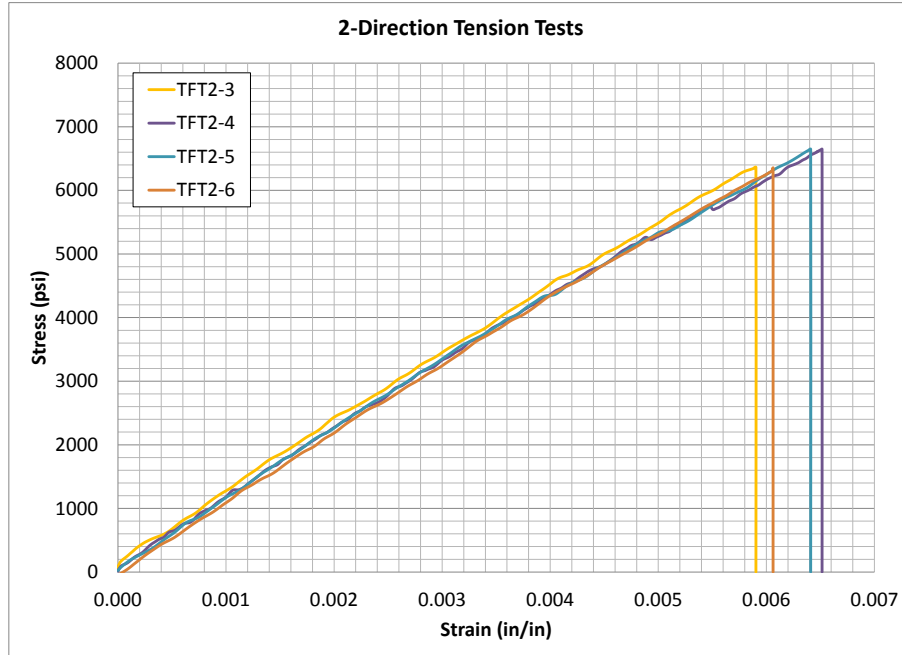


Fig. 1. 2-direction tension curves

Table 1. 2-Direction Tension Summary of Results

Replicate	Loading Rate (in/min)	E <sub>22</sub> (psi)	Poisson's Ratio (ν <sub>21</sub> )	Ultimate Strain	Peak Stress (psi)
TFT2-3	0.005	1 055 484	0.0156	0.00590	6 360
TFT2-4	0.0025	1 076 171	0.0155	0.00652	6 647
TFT2-5	0.005	1 069 788	0.0185	0.00641	6 646
TFT2-6	0.005	1 082 595	0.0177	0.00606	6 356
Average		1 066 413	0.0168	0.00622	6 502
Standard Deviation		14 087	0.0015	0.00029	167
Coefficient of Variation		1.3%	9.0%	4.6%	2.6%

### 3-Direction Compression

The specimen geometry and layout are shown in Fig. 3. The results are summarized in Fig. 4 and Table 3.

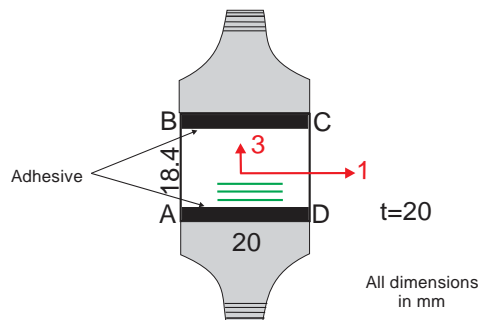


Fig. 3. 3-direction compression test specimen

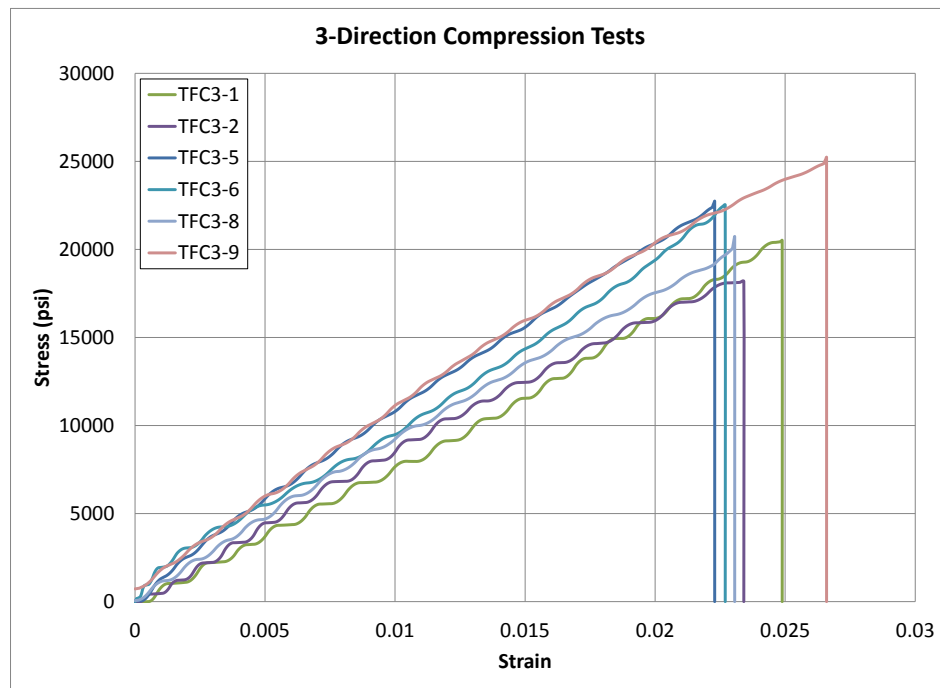


Fig. 4. 3-direction compression curves

Table 2. 3-Direction Compression Summary of Results

Replicate	Loading Rate (in/min)	E <sub>33</sub> (psi)	Failure Strain	Peak Stress (psi)
TFC3-1	0.01	829 721	0.02489	20 514
TFC3-2	0.01	881 691	0.02341	18 184
TFC3-5	0.01	974 307	0.02229	22 751
TFC3-6	0.01	933 158	0.02270	22 531
TFC3-8	0.01	842 045	0.02306	20 742
TFC3-9	0.01	1 004 352	0.02659	25 247
Average		910 879	0.02382	21 662
Standard Deviation		71 321	0.00162	2411
Coefficient of Variation		7.8%	6.8%	11.1%

### 1-3 Plane Shear

The specimen geometry and layout are shown in Fig. 5. The results are summarized in Fig. 5 and Table 4.

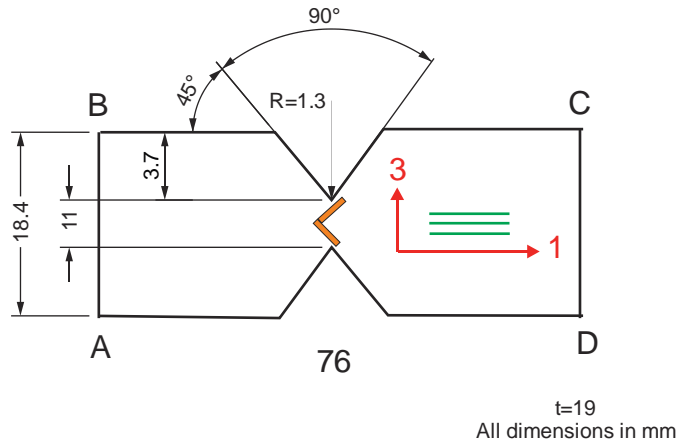


Fig. 5. 1-3 plane shear specimen orientation

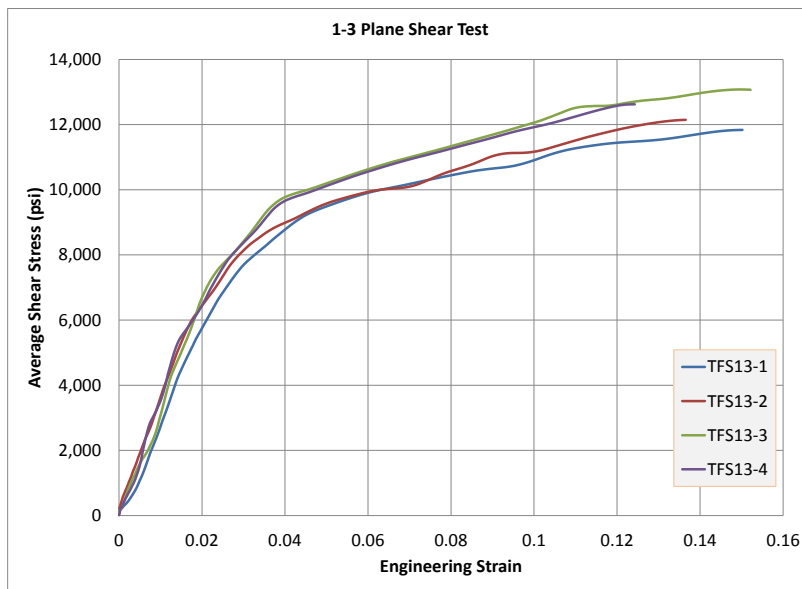


Fig. 6. 1-3 plane shear curves

Table 4. 1-3 Plane Shear Summary of Results

Replicate	Loading Rate (in/min)	G <sub>13</sub> (psi)	Failure Strain	Peak Stress (psi)
TFS13-1	0.05	345 941	0.15022	11 837
TFS13-2	0.05	341 301	0.13654	12 146
TFS13-3	0.05	358 760	0.15216	13 070
TFS13-4	0.04	344 951	0.12427	12 623
Average		347 738	0.14079	12 419
Standard Deviation		7 614	0.01303	541
Coefficient of Variation		2.2%	9.3%	4.4%

### Determination of Additional Input Parameters

The flow rule coefficients can be calculated using the flow law from Eqn. (8) and using the Poisson's ratio of the plastic strains to derive a set of functions relating the flow rule coefficients to the plastic Poisson's ratios obtained from the experiments described above. A general form of these equations can be rewritten in terms of the plastic Poisson's ratios and  $H_{11}$  as

$$\begin{aligned}
 H_{12} &= -\nu_{12}^p H_{11} = -\nu_{12}^p \\
 H_{13} &= -\nu_{13}^p H_{11} = -\nu_{13}^p \\
 H_{22} &= \frac{\nu_{12}^p}{\nu_{21}^p} H_{11} = \frac{\nu_{12}^p}{\nu_{21}^p} \\
 H_{23} &= \frac{-\nu_{23}^p \nu_{12}^p}{\nu_{21}^p} H_{11} = \frac{-\nu_{23}^p \nu_{12}^p}{\nu_{21}^p} \\
 H_{33} &= \frac{\nu_{13}^p}{\nu_{31}^p} H_{11} = \frac{\nu_{13}^p}{\nu_{31}^p}
 \end{aligned} \tag{9}$$

but requires a known value of  $H_{11}$ . However, in the case of a unidirectional carbon fiber composite, it is reasonable to assume that the plastic strain in the fiber direction (1 direction) is equal to zero for all values of stress, due to the linear elastic behavior of the carbon fiber, also discussed by Sun and Chen (Sun, et al., 1989). From the second expression in Eqn. (8), it is clear that the plastic strain can only be zero if the flow law coefficients  $H_{11}$ ,  $H_{12}$ , and  $H_{13}$  are all equal to zero. In the same regard, the response in the transverse (2-direction) composite direction shows some degree of nonlinearity, and for a unidirectional load in the 2 direction, it is reasonable to assume the value of the effective stress,  $h$ , to be equal to the applied stress,  $\sigma_{22}$ . Then, the plastic potential function, Eqn. (7), can be simplified for the case of a uniaxial applied load in the 2-direction as

$$h = \sqrt{H_{22} \sigma_{22}^2} = \sqrt{H_{22}} \sigma_{22}, \tag{10}$$

and from the assumption that the effective stress,  $h$ , in this case, is equal to the applied stress,  $\sigma_{22}$ , the flow law coefficient,  $H_{22}$ , must be equal to one. Due to the transverse isotropy in the unidirectional composite, the flow law coefficient,  $H_{33}$ , can be assumed to be one as well, and using these known values of the flow law coefficients, the remaining value,  $H_{23}$ , can be determined using the plastic Poisson's ratio in the 2-3 plane (uniaxial loading in the 2-direction,  $\sigma_{22} \neq 0$ ) as

$$\nu_{23}^p = -\frac{\dot{\epsilon}_{33}^p}{\dot{\epsilon}_{22}^p} = \frac{2H_{13}\sigma_{11} + 2H_{23}\sigma_{22} + 2H_{33}\sigma_{33}}{2H_{12}\sigma_{11} + 2H_{22}\sigma_{22} + 2H_{23}\sigma_{33}} = -\frac{H_{23}}{H_{22}}$$

$$H_{23} = -H_{22} \nu_{23}^p = -\nu_{23}^p \tag{11}$$

which is equal to the negative value of the plastic Poisson's ratio,  $\nu_{23}^p$ . The flow law coefficients are assumed to be constant, which requires a constant value of the plastic Poisson's ratio, and was determined as an average value from unidirectional transverse (2-direction) tension test data.

The final three flow law coefficients  $H_{44}, H_{55}$  and  $H_{66}$ , are determined using the same fit technique as in the simplified case (Goldberg et al., 2015), but each shear curve must be fit with the 2-direction test acting as the baseline. These are calculated by fitting the effective stress versus effective plastic strain curves of the shear tests with the master uniaxial test. In order to fit the shear curves with the uniaxial curve, to find the optimal flow rule coefficient value, the difference in the curves is minimized as

$$f(H_{ll}) = \sum_{k=1}^n \left[ (\hat{\sigma}_{22})_k - (\hat{\sigma}_{ij})_k \right]^2 \tag{12}$$

such that

$$H_{ll}^{\min} \leq H_{ll}^* \leq H_{ll}^{\max}$$

where  $n$  is the number of data points on the master curve,  $(\hat{\sigma}_{ii})_k$  is the  $k^{\text{th}}$  effective stress value from the master curve and  $(\hat{\sigma}_{ij})_k$  is the effective stress value for the shear curve, given a value of  $H_{ll}$  used in Eqn. (7). Results from computing the optimal flow-rule coefficients (solution to Eqn. (12)) are shown in Fig. 7 and Fig. 8, with  $H_{44} = H_{66} = 7.7$  and  $H_{55} = 6.1$ .

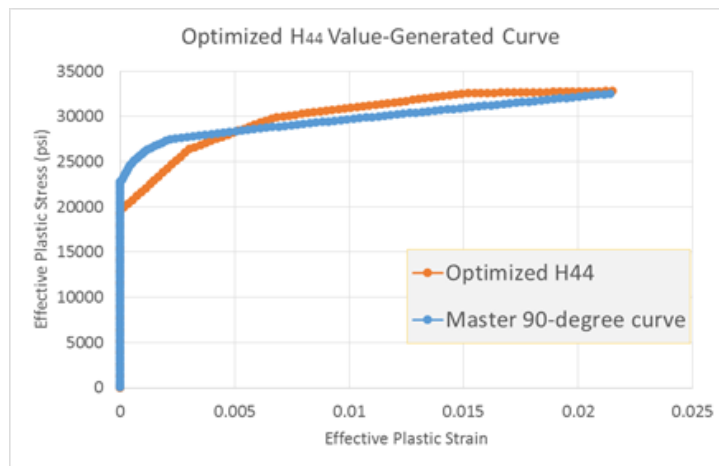


Fig. 7. Comparison of master curve with optimized H44 (and H66) value

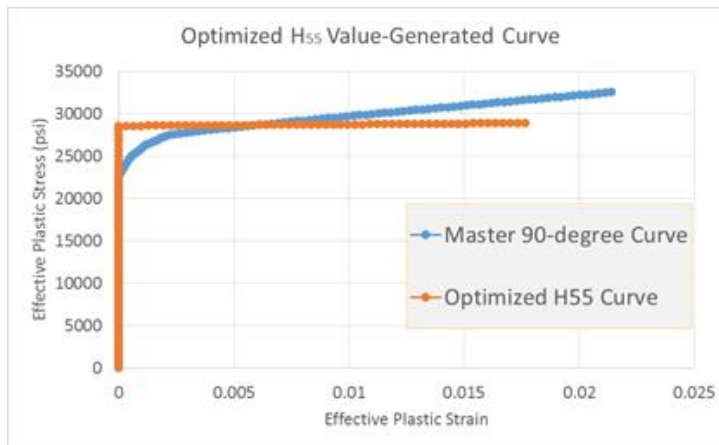


Fig. 8. Comparison of master curve with optimized H55 value

## Validation Test

Validation of the MAT213 material model was performed using a ballistic plate impact test. The plate is made of the T800/F3900 unidirectional composite described earlier. The panel has dimensions of 12" x 12" x 0.122". Fig. 9 shows the experimental test setup (Fig. 9(a)) that includes the aluminum impactor geometry (Fig. 9(c)-(d)).

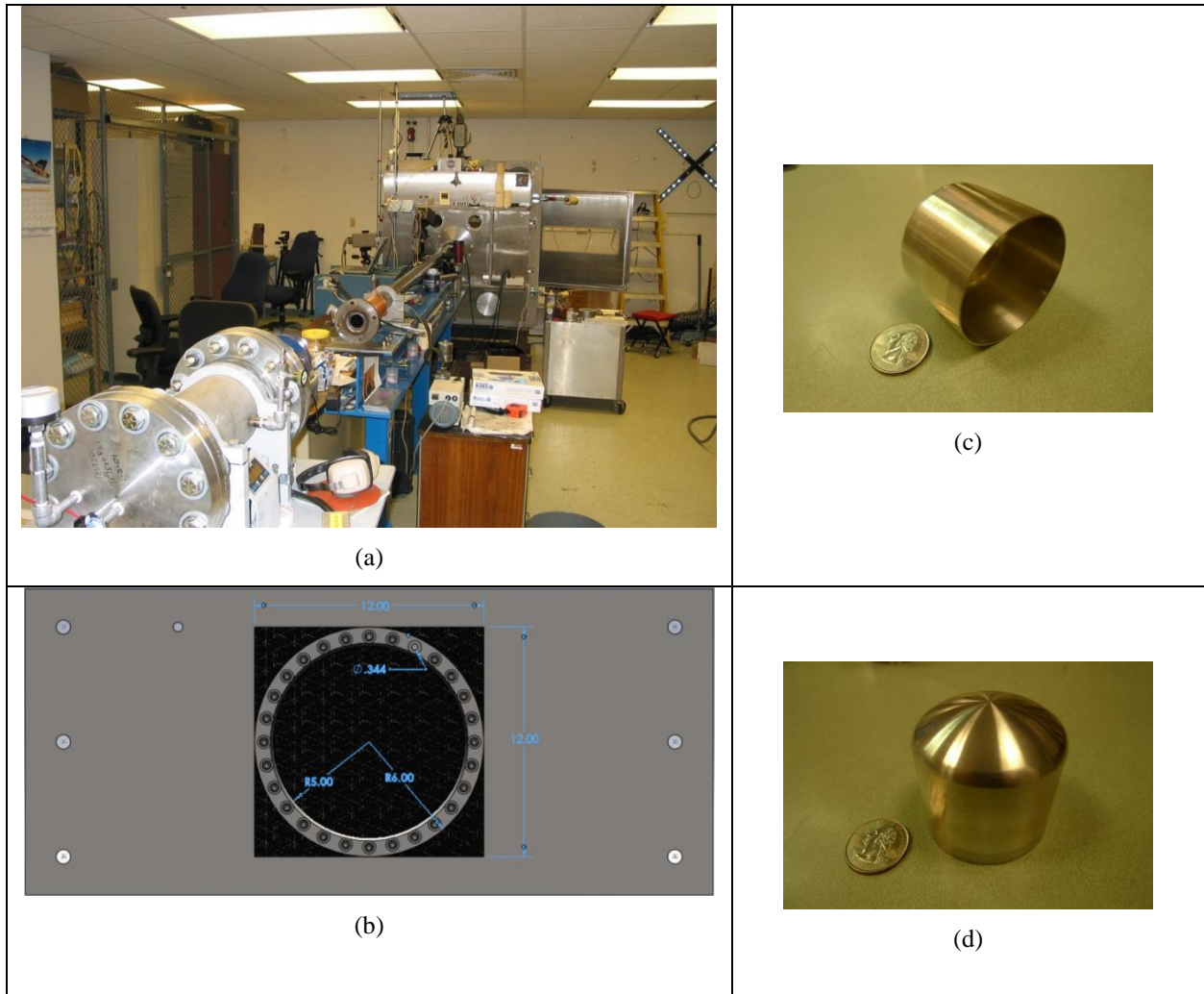


Fig. 9. Impact Structural Test (a) Small impact gun (b) 12" x 12" panel with a 10" circular clamping pattern (c) 50 gm Hollow Al-2024 projectile with radiused front face (d) Another view of the projectile

The impact velocity of the projectile was recorded as 27.4 ft/s. Digital image correlation (DIC) was used to track the out-of-plane (z-direction) displacement and in-plane strains on the entire back surface of the plate. To simulate the impact test, a finite element model was created (Fig. 10).

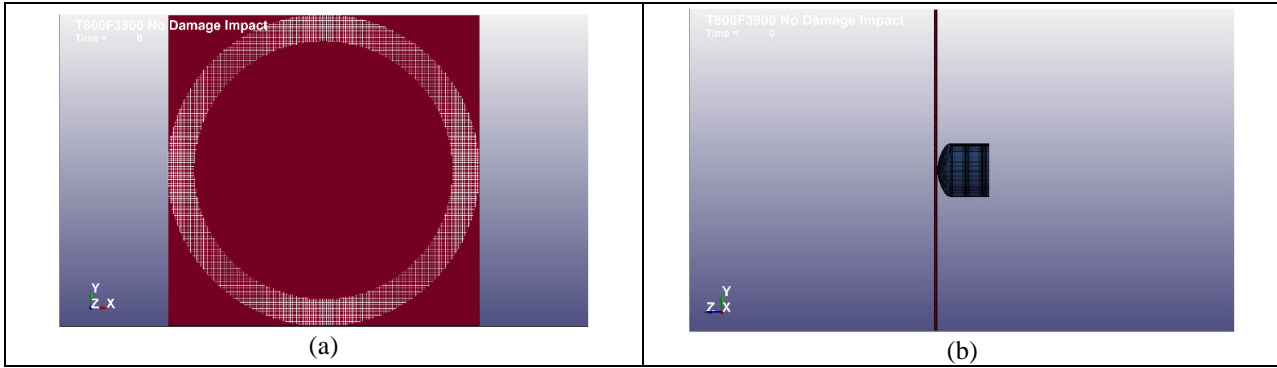


Fig. 10. LS-DYNA finite element model (a) back view, (b) side view

The plate in the finite element model is represented by 288,000 8-noded hexahedral elements with 5 elements through the thickness, resulting in element dimensions of 0.05” x 0.05” x 0.0244”. The projectile is modeled using 27,200 8-noded hexahedral elements. For comparison, two material models were used to define the plate, including the previously described MAT213 as well as MAT22. The projectile is modeled as aluminum using MAT24. The material properties used for the MAT22 and MAT24 models are listed in Table 5 and Table 6, respectively.

Table 5. MAT22 Material Parameters

Model Parameter	Value
Mass density (lb-s <sup>2</sup> /in)	1.4507(10 <sup>-4</sup> )
E <sub>a</sub> (psi)	21.83(10 <sup>6</sup> )
E <sub>b</sub> (psi)	1.145(10 <sup>6</sup> )
E <sub>c</sub> (psi)	1.145(10 <sup>6</sup> )
<i>v</i> <sub>ba</sub>	0.01385
<i>v</i> <sub>ba</sub>	0.01385
<i>v</i> <sub>ba</sub>	0.3792
G <sub>ab</sub> (psi)	0.5796(10 <sup>6</sup> )
G <sub>bc</sub> (psi)	0.3243(10 <sup>6</sup> )
G <sub>ca</sub> (psi)	0.5796(10 <sup>6</sup> )
Shear Strength, SC (psi)	0.01376(10 <sup>6</sup> )
Longitudinal Tensile Strength, XT (psi)	0.412(10 <sup>6</sup> )
Transverse Tensile Strength, YT (psi)	0.00872(10 <sup>6</sup> )
Transverse Compressive Strength, YC (psi)	0.0243(10 <sup>6</sup> )
Alpha	0.0
Normal Tensile Strength, SN (psi)	0.00872(10 <sup>6</sup> )
Transverse Shear Strength, SYZ (psi)	0.015(10 <sup>6</sup> )
Transverse Shear Strength, SZX (psi)	0.01376(10 <sup>6</sup> )

Table 6. MAT24 Material Properties

Model Parameter	Value
Mass density (lb-s <sup>2</sup> /in)	2.539(10 <sup>-4</sup> )
E	10.30(10 <sup>6</sup> )
<i>v</i>	0.334
Yield Stress, SIGY	42500
Tangent Modulus, ETAN	42000

Comparison of the finite element simulations and the experimental results was carried out using the out-of-plane displacement on the back surface of the plate while studying both the surface contour plot as well as the time history associated with the point where the maximum Z-displacement occurred. The contour plots are compared in Fig. 11, with the finite element results shown for the same time of 0.0007s and all scales matching; noting that Fig. 11(a) shows the initial impact time of the experimental test. It can be seen that the MAT213 results (Fig. 11(d))

show a more rounded contour of the out-of-plane displacements than that seen in the MAT22 results (Fig. 11(c)) and represents the experimental results (Fig. 11(b)) more accurately.

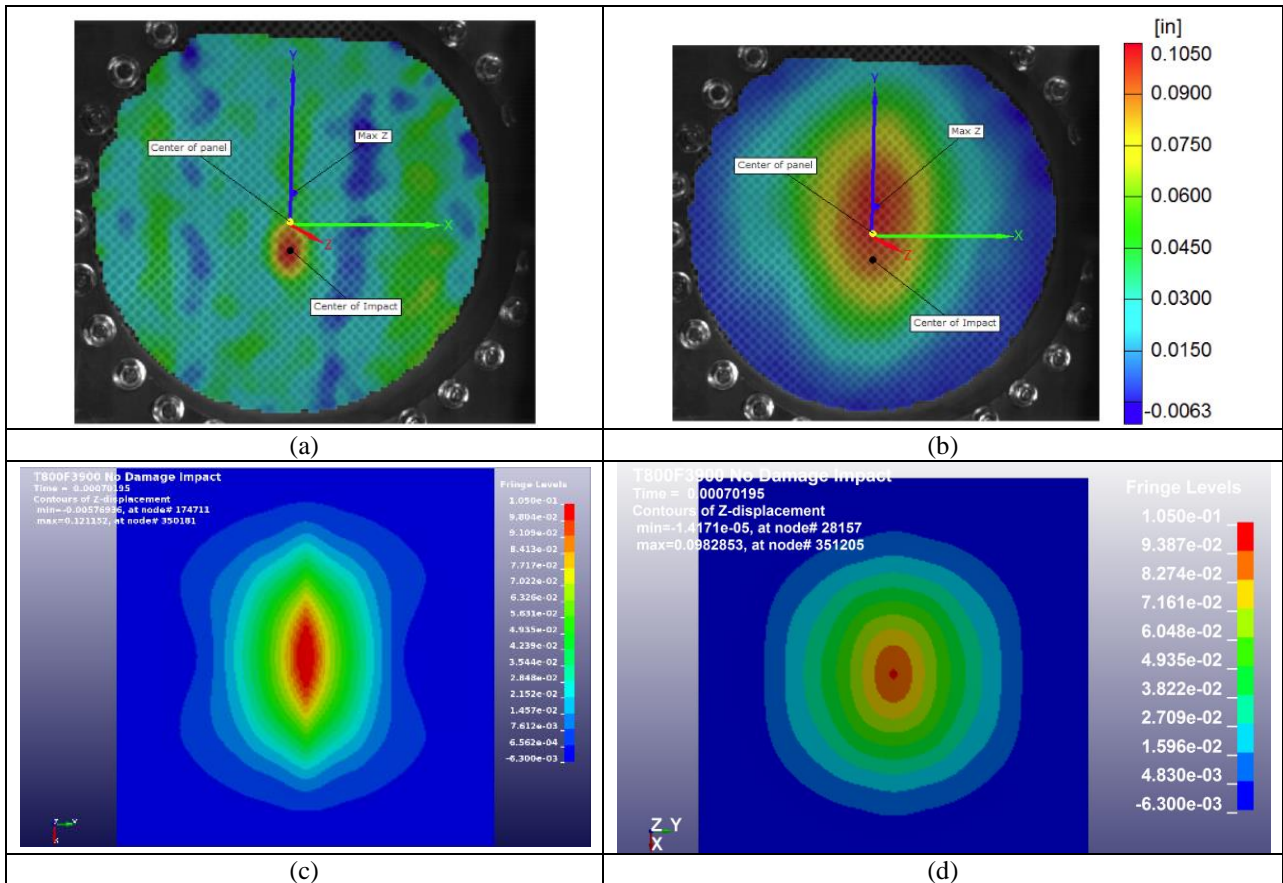


Fig. 11 (a) Plot of experimental data showing center of panel, point of impact and location of the max. Z-displacement; Out-of-plane displacement contours at t=0.0007s for (b) experiment (c) MAT22 simulation and (d) MAT213 simulation

A plot of the out-of-plane displacements as a function of time is shown in Fig. 12, with the experimental test results reported at the center of the plate as well as the point of maximum displacement. The displacement versus time results of the MAT213 simulation more closely match the experimental center compared with the MAT22 simulation. It should be noted that there is no damping included in the finite element models.

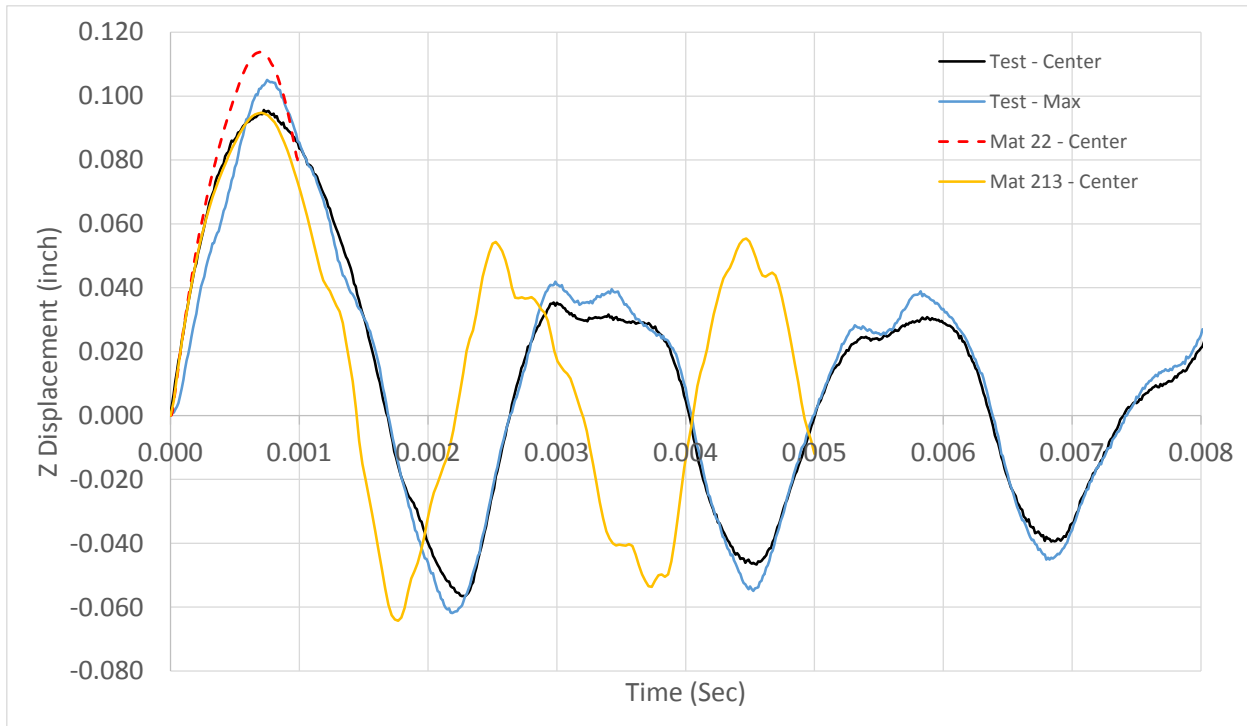


Fig. 12. Maximum out-of-plane (Z) displacement versus time plot for the impact test, and MAT22 and MAT213 simulations. In addition, the Z-displacement at the center of the plate for the impact test is also shown.

## Conclusions

An orthotropic elasto-plastic-damage three-dimensional model with tabulated input has been developed to analyze the impact response of composite materials and implemented into a tailored version of LS-DYNA. Preliminary results show that the material model can accurately represent the deformation of the model. Ongoing work include adding other desirable features such as damage and failure models, and rate and temperature dependencies.

## Acknowledgements

Authors Hoffarth, Khaled and Rajan gratefully acknowledge the support of (a) the Federal Aviation Administration through Grant #12-G-001 titled “Composite Material Model for Impact Analysis”, William Emmerling, Technical Monitor, and (b) NASA through Contract Number: NN15CA32C titled “Development and Implementation of an Orthotropic Plasticity Progressive Damage Model for Transient Dynamic/Impact Finite Element Analysis of Composite Structures”, Robert Goldberg, Contracting Officer Representative.

## References

ASTM D 792-13 Committee (2013). Standard Test Methods for Density and Specific Gravity (Relative Density) of Plastics by Displacement, ASTM International, West Conshohocken, PA.

ASTM D 7291/D7291M-07 Committee (2007). Test Method for Through-Thickness “Flatwise” Tensile Strength and Elastic Modulus of a Fiber-Reinforced Polymer Matrix Composite Material, ASTM International, West Conshohocken, PA.

ASTM D 3410/D3410M-03 Committee (2008). Test Method for Compressive Properties of Polymer Matrix Composite Materials with Unsupported Gage Section by Shear Loading, ASTM International, West Conshohocken, PA.

ASTM D 3039/D3039M Committee (2014). Test Method for Tensile Properties of Polymer Matrix Composite Materials, ASTM International, West Conshohocken, PA.

ASTM D 5379/D5379M-12 Committee (2013). Test Method for Shear Properties of Composite Materials by the V-Notched Beam Method, ASTM International, West Conshohocken, PA.

ASTM D 7078/D7078M-12 (2012). Standard Test Method for Shear Properties of Composite Materials by V-Notched Rail Shear Method, ASTM International, West Conshohocken, PA.

Goldberg, R., Carney, K., DuBois, P., Hoffarth, C., Harrington, J., Rajan, S.D. and Blankenhorn, G. (2015). "Development of an Orthotropic Elasto-Plastic Generalized Composite Material Model Suitable for Impact Problems", ASCE J of Aerospace Engineering, DOI: 10.1061/(ASCE)AS.1943-5525.0000580.

Harrington, J., Hoffarth, C., Rajan, S.D., Goldberg, R., Carney, K., DuBois, P., and Blankenhorn, G. (2016). "Using Virtual Tests to Complete the Description of a Three-Dimensional Orthotropic Material", manuscript in preparation.

Hoffarth, C., Rajan, S.D., Goldberg, R., Carney, K., DuBois, P. and Blankenhorn, G. (2016). Implementation and Validation of a Three-Dimensional Material Model for Orthotropic Composites, submitted to Composites B.

Sun, C. T., and J. L. Chen. 1989. "A Simple Flow Rule for Characterizing Nonlinear Behavior of Fiber Composites." *Journal of Composite Materials* 23: 1009:1020.

Toray Carbon Fibers America (2003). T800S Data Sheet (Technical Data Sheet No. CFA-019), accessed from [www.toraycfa.com/pdfs/T800SDataSheet.pdf](http://www.toraycfa.com/pdfs/T800SDataSheet.pdf).